Identification and Localization of Cyanophycin in Bacteria Cells via Imaging of the Nitrogen Distribution Using Energy-Filtering Transmission Electron Microscopy

Anne Koop,[†] Ingo Voss,[‡] Andreas Thesing,[†] Helmut Kohl,[†] Rudolf Reichelt,[§] and Alexander Steinbüchel*,[‡]

Physikalisches Institut und Interdisziplinäres Centrum für Elektronenmikroskopie und Mikroanalyse, Westfälische Wilhelms-Universität Münster, Wilhelm-Klemm-Straβe 10, D-48149 Münster, Germany, Institut für Molekulare Mikrobiologie und Biotechnologie, Westfälische Wilhelms-Universität Münster, Corrensstraβe 3, D-48149 Münster, Germany, and Institut für Medizinische Physik und Biophysik, Universitätsklinikum Münster, Westfälische Wilhelms-Universität Münster, Robert-Koch-Straβe 31, D-48149 Münster

Received November 27, 2006; Revised Manuscript Received May 3, 2007

In this study the technique of energy-filtering transmission electron microscopy was applied to localize cyanophycin (CGP) in recombinant strains of *Ralstonia eutropha*. Since CGP is a polymer consisting of the amino acids aspartate and arginine, which functions as a temporary nitrogen reserve that is deposited as insoluble inclusions in the cytoplasm of the cell, its nitrogen content is significantly higher than that of the other cell matter. In this study, we recorded nitrogen distribution maps, which represent the location of CGP in ultrathin sections of resin-embedded cells of recombinant strains of *R. eutropha* expressing the cyanophycin synthetase of *Anabaena* sp. strain PCC 7120. Furthermore, the existence of nitrogen in CGP granules was additionally proven by recording electron energy-loss spectra. The samples of *R. eutropha* H16 (pBBR1MCS-2::*cphA1*$_{7120}$) revealed a second type of granule, which does not show nitrogen in the corresponding maps and which can be identified as an inclusion containing poly(3-hydroxybutyric acid). The methods applied in this study are suitable to identify storage compounds with elevated nitrogen contents and to reveal their location in the bacterial cell. The methods are also very helpful to distinguish between inclusions of different chemical compositions that occur both at the same time in the cells but cannot or only hardly be distinguished by other methods.

Introduction

Cyanophycin (multi-L-arginyl-poly[L-aspartic acid]), also referred to as cyanophycin grana protein (CGP), is a non-ribosomally synthesized protein-like polymer that was discovered about 120 years ago in cyanobacteria.[1] The polymer consists typically of equimolar amounts of aspartic acid and arginine, and its proposed chemical structure is a poly-α-aspartic acid backbone with arginine residues linked to the β-carboxyl groups of aspartic acid by isopeptide bonds.[2] In nature, CGP is produced by most cyanobacteria[3−9] and the chemotrophic bacterium *Acinetobacter* sp. strain DSM 587.[10] CGP functions as a temporary nitrogen, carbon, and energy reserve. It accumulates during the transition from the exponential to the stationary growth phase and disappears when balanced growth resumes.[11] At neutral pH and physiological ionic strength, CGP is insoluble and deposited in the cytoplasm as membraneless granules.[9]

CGP is of biotechnological interest because the purified polymer can be chemically converted into a polymer with reduced arginine content,[12,13] which might be used like polyaspartic acid as a biodegradable substitute for the non-biodegradable synthetic polyacrylate in various technical processes.[14] In addition, it might also be of interest for other applications if the unknown physical and material properties of this polymer are revealed.

Polymerization and degradation of this polyamide in cyanobacteria are catalyzed by cyanophycin synthetase and cyanophycinase, respectively. Both enzymes are encoded by consecutive genes within a cluster, *cphA* for cyanophycin synthetase and *cphB* for cyanophycinase. The *cphA* genes from *Anabaena variabilis* ATCC 29413,[15] *Anabaena* sp. strain PCC 7120,[16] *Synechocystis* sp. strain PCC 6803,[17] *Synechocystis* sp. strain PCC 6308,[18] *Synechococcus elongatus*,[19] *Synechococcus* sp. strain MA19,[20] as well as from the chemotrophic bacteria *Acinetobacter* sp. strain DSM 587[10] or *Desulfitobacterium hafniense* DCB-2[21] were cloned and expressed in *Escherichia coli*. More recently, heterologous expression of *cphA* was also demonstrated in recombinant strains of *Ralstonia eutropha*, *Corynebacterium glutamicum*, *Pseudomonas putida*, and *Bacillus megaterium*.[16,22] Recombinant strains of *R. eutropha* expressing *cphA1* of *Anabaena* sp. strain PCC 7120 accumulated CGP up to 22.0% (w/w) of the cellular dry weight (CDW), which is significantly higher than the value conferred to *R. eutropha* by other cyanobacterial *cphA* genes.[16] Whereas in cyanobacteria the molecular mass of the polymer ranged from 25 to 100 kDa,[7] the polymer from recombinant strains harboring *cphA* exhibited a molecular weight ranging from 25 to 30 kDa only; furthermore, lysine occurred as an additional amino acid in the isolated polymer thereby partly replacing arginine.[15,16,22]

In this study, we report on a new in situ method to identify and localize CGP within the cells using energy-filtering

* Author to whom correspondence should be addressed. Phone: +49-251-8339821. Fax: +49-251-8338388. E-mail: steinbu@uni-muenster.de.
[†] Physikalisches Institut und Interdisziplinäres Centrum für Elektronenmikroskopie und Mikroanalyse.
[‡] Institut für Molekulare Mikrobiologie und Biotechnologie.
[§] Institut für Medizinische Physik und Biophysik.

10.1021/bm0611230 CCC: $37.00
Published on Web 08/22/2007

Table 1. Bacterial Strains and Plasmids Used in This Study[a]

strains or plasmids	relevant characteristics	reference or source
	Strains of *Ralstonia eutropha*	
H16	wild-type	DSM 428
H16-PHB$^-$4	mutant of H16 defective in the synthesis of PHA	ref 44, DSM 541
	Plasmids	
pBBR1MCS-2	Km^r, broad host range vector, *lacPOZ'*	ref 45
pBBR1MCS-2:: *cphA1*$_{7120}$	pBBR1MCS-2 harboring *cphA1* from *Anabaena* sp. strain PCC7120 colinear to *lacPOZ'*	ref 16

[a] DSM, Deutsche Sammlung von Mikroorganismen und Zellkulturen, Braunschweig, Germany; PCC, Pasteur Culture Collection of Cyanobacteria, Paris, France. Km, kanamycin, *cphA*$_x$, source of cyanophycin synthetase gene.

transmission electron microscopy (EFTEM). Selecting the slit width and position in the energy filter allowing those electrons to contribute, which were scattered inelastically by exciting or ionizing a nitrogen K-shell, with subsequent subtraction of an element-unspecific background, we obtained an element distribution image of nitrogen in the cytoplasm. The technique for recording and calculating element distribution images was described in more detail previously.[23,24] Since CGP contains nitrogen in a higher concentration than the dry matter of the bacterial cells, such an elemental map can be used to localize CGP in the cells. For the preparation of the specimens, the cells were embedded in Spurr and stained with uranyl acetate. We analyzed electron energy-loss (EEL) spectra of these materials to ensure that they do not influence the nitrogen distribution images by a possible nitrogen share of their own. This method will beside various light and electron microscopic methods provide an additional method to identify CGP granules in situ in cells.

Experimental Section

Bacterial Strains, Plasmids, and Culture Conditions. The bacterial strains and plasmids used in this study are listed in Table 1. Strains of *R. eutropha* were cultivated in Erlenmeyer flasks without baffles in mineral salts medium (MSM) according to Schlegel and co-workers.[25] Sodium gluconate was used as carbon source at concentrations of 1−2% (w/v), and aspartic acid and arginine were added as supplements at concentrations of 0.2% (w/v) to enhance synthesis and accumulation of CGP in recombinant strains of *R. eutropha* expressing *cphA* from *Anabaena* sp. strain PCC 7120. For selection of plasmid carrying strains, kanamycin was added to the medium at a concentration of 300 μg/mL. The flasks were incubated at 30 °C and 150 rpm on a Pilotshake RC-4/6-W horizontal shaker (Kühner AG, Birsfelden, Switzerland) for 48 h.

For heterologous expression of *cphA1* from *Anabaena* sp. strain PCC 7120 in *R. eutropha* the previously constructed plasmid pBBR1MCS-2::*cphA1*$_{7120}$ was used,[16] which was transferred into *R. eutropha* by conjugation using *E. coli* S17-1 as a donor strain.[26]

Preparation of Cells for EFTEM. The bacterial cells were fixed with 2.5% (v/v) glutardialdehyde in 0.1 M sodium phosphate buffer (SPB; pH 7.3) according to Sørensen for 45 min.[27] After being washed three times with SPB for 15 min each, the cells were postfixed in 1% (w/v) osmium tetroxide in 0.1 M SPB (pH 7.3). Then the water was removed by a graded water−ethanol series (30%, 50%, 70%, 90%, 96%, and two times with absolute ethanol) and finally by propylene oxide each for approximately 15 min. Subsequently, the cells were embedded in Spurr resin[28] polymerized at 70 °C for at least 8 h. Ultrathin sections were made from the embedded samples with the Ultracut S (Reichert Ltd., Austria) using a diamond knife. The ultrathin sections were placed onto Cu mesh grids and then stained by uranyl acetate (saturated aqueous solution). Ultrathin sections of polymerized Spurr without cells were also made for some control experiments to check for the purity of the embedding resin.

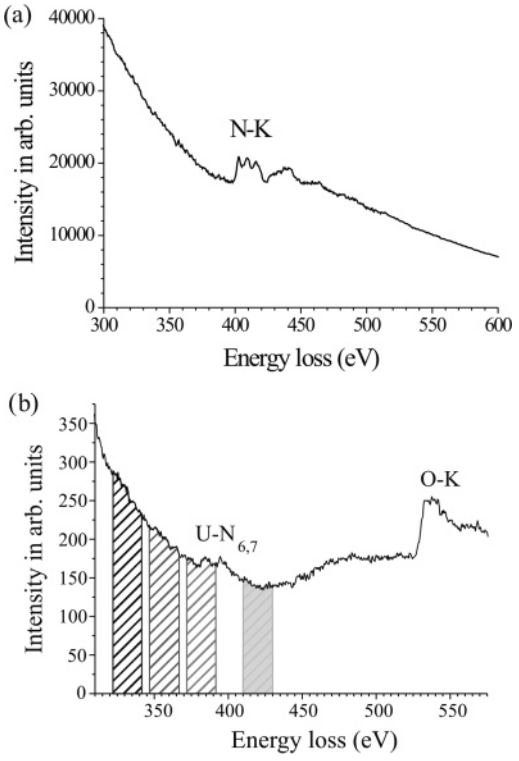

Figure 1. Examples for EEL spectra: (a) EEL spectrum of a boron nitride sample with a nitrogen K-edge taken from ref 29; (b) EEL spectrum of uranyl acetate. The hatched areas represent the energy-loss windows selected for the preedge images and the nitrogen-sensitive image.

Analytical Electron Microscopy: EEL Spectroscopy. Employing an electron microscope equipped with an imaging energy filter, electrons, which have been scattered in the specimen, can be detected as a function of the energy loss suffered in the specimen. At higher-energy losses the EEL spectrum shows pronounced ionization edges. These are caused by electrons, which have excited a tightly bound inner-shell electron into the continuum.

In the literature abbreviations are used for the nomenclature of the ionization edges. These abbreviations contain the abbreviation of the element name (e.g., C for carbon, O for oxygen, N for nitrogen, and U for uranium) and the type of atomic shell, which was ionized by the incoming electron (e.g., K for a K-shell, L for a L-shell, etc). If the abbreviation of the considered shell contains an index, then this index defines the subshell that has been ionized.

Examples of ionization edges of nitrogen and uranium in EEL spectra are shown in Figure 1. The EEL spectrum from the nitrogen K-edge stems from a boron nitride sample and was taken from a reference handbook.[29] The EEL spectrum of uranium was recorded from an uranyl acetate sample and will be discussed below. The characteristic energy loss of the ionization edge onset and the characteristic form of the edge in an EEL spectrum can be used to identify the chemical elements in the specimen area illuminated by the electron beam. Also a quantitative determination of the concentration of the elements contained in the illuminated specimen area is possible by analyzing ionization edges in an EEL spectrum.

For this purpose the element-unspecific background at an ionization edge has to be determined and subtracted. We use the power law model for the determination of the background

$$I_B(E) = AE^{-r} \quad (1)$$

with E representing the energy loss and A and r the two fit parameters.[30]

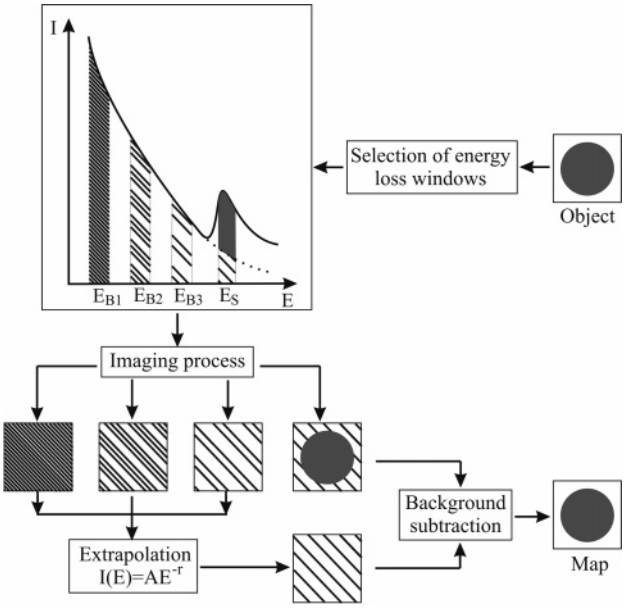

Figure 2. Schematic illustration of the recording of elemental maps using three preedge images and one element-specific image. The preedge images are recorded at energy losses E_{B1}, E_{B2}, and E_{B3}, and the element-specific image at the energy loss E_S within the ionization edge of the element of interest.

These are determined by performing a least-squares fit of the intensity in the preedge region below the ionization edge of interest. For thin specimens the intensity of a the background-corrected ionization edge of the element "a" within an energy-loss interval $[E_a, E_a + \Delta E]$ in an EEL spectrum can be expressed by eq 2[31]

$$I_a(E_a, \Delta E, \vartheta_a) = I_0 n_a \sigma_a(E_a, \Delta E, \vartheta_a) \quad (2)$$

Here n_a is the projected particle density of atoms "a" within the illuminated specimen volume, whereas I_0 represents the number of incoming electrons. The term $\sigma_a(E_a, \Delta E, \vartheta_a)$ represents the cross-section for the corresponding inner-shell excitation, in which the energy loss of an electron lies within the energy-loss interval $[E_a, E_a + \Delta E]$ and the scattering angle of the electron is smaller than the aperture half angle ϑ_a.

Analytical Electron Microscopy: Element Distribution Images. The imaging energy filter in an energy-filtering transmission electron microscope permits the recording of element distribution images or elemental maps, yielding two-dimensional projected chemical information about the distribution of an element of interest. Setting an energy slit in the electron dispersive plane of the imaging energy filter, only those electrons are selected for a contribution to the image that have been inelastically scattered in the specimen suffering an energy loss within the energy-loss interval $[E_w - \Delta E/2, E_w + \Delta E/2]$. Detailed descriptions of the technique of recording and calculating element distribution images are given in standard textbooks.[23,24,30] The background from at least two preedge images must be determined and subtracted pixel by pixel in the image to obtain an element distribution image with an intensity I_S and referring to an element "a".

We have used three preedge images as schematically shown in Figure 2. Additionally, we have calculated the signal-to-noise ratio (SNR) for each pixel following well-known procedures.[32−34] If one has previous knowledge that the element of interest is contained in the sample, then the existence of this element is regarded as proven in a pixel of an element distribution image, when the pixel has a SNR ≥ 3. Otherwise, when no previous knowledge exists about the element of interest in the specimen, a SNR ≥ 5 is needed for the identification of this element in a pixel.[35,36] In this Rose criterion the pixels are regarded as independent.

Identification of CGP by Using EFTEM. This study aimed at the identification of CGP in recombinant strains of *R. eutropha*. The empirical formula of the CGP dipeptide building block is $C_{10}H_{17}N_5O_4$. The mass distribution of elements in the dried polymer is given by 44.3% C, 25.8% N, 23.6% O, and 6.3% H, while the distribution of elements referring to the number of atoms resulting from the empirical formula is 27.8% C, 47.2% H, 13.9% N, and 11.1% O. There is no knowledge so far about further elements occurring, for example, as counterions in the polymer.

One of the strains to be analyzed is a recombinant strain of the wild-type *R. eutropha* H16 harboring plasmid pBBR1MCS-2::*cphA1*$_{7120}$. The cells of this strain store CGP and additionally poly(3-hydroxybutyric acid) (PHB). PHB consists of polymerized carboxylic acid esters, which are responsible for the lipophilic or hydrophobic properties of the material. PHB does not contain nitrogen. It accumulates in cells in the form of granules, which are surrounded by a membrane.[37] Furthermore, CGP shall be identified in the recombinant strain of the mutant *R. eutropha* H16-PHB$^-$4 (pBBR1MCS-2::*cphA1*$_{7120}$), which only stores CGP. PHB cannot be produced by these cells, because PHB synthesis is impaired due to mutation.

The mass distribution of elements in the bacterial cell dry matter, which does not contain CGP, is 50% C, 20% O, 14% N, 8% H, 3% P, 1% S, 1% Na, 1% K, 0.5% Mg, 0.5% Cl, 0.5% Ca, and 0.2% Fe. The distribution of elements in atomic percent is given by 28.4% C, 8.5% O, 6.8% N, and 54.6% H, neglecting here the elements with a share of less than 1%. Comparing the chemical composition of CGP and the cell dry matter without CGP shows a strong difference in the nitrogen concentration. Therefore, the recording of nitrogen distribution images via EFTEM using the method described above should yield images in which the CGP inclusions are visible within the cells due to the noticeably higher nitrogen concentration of CGP in comparison to that of the surrounding cell matter.

Theoretical Background, Experimental Conditions, and Preparatory Measurements. The measurements presented here were carried out on a Zeiss EM 902 transmission electron microscope with an acceleration voltage of 80 kV and equipped with a Castaing-Henry imaging energy filter. The images were recorded with a slow scan charge coupled device (CCD) camera (model Gatan MSC 794), and the EEL spectra were detected serially with a scintillator−photomultiplier combination below the final image plane.

Specimen Preparation. During the preparation of the specimens, the cells were stained with uranyl acetate ($UO_2(C_2H_3O_2)_2 \cdot 2H_2O$), and the embedding material Spurr[28] was used. Consequently, not only the bacterial cells but also these materials contribute to the images and EEL spectra recorded by EFTEM. We recorded EEL spectra of these materials to analyze their chemical composition and to ensure that they neither contained nitrogen nor impurities, which would make it more difficult to draw reliable information about the nitrogen distribution in bacterial cells from the nitrogen distribution images.

Spurr is made of the components ERL-4206, DER 736, NSA, and S1.[28] The fraction of S1 is very small in comparison to those of the other three components, and the dimethylaminoethanol molecule of S1 contains only one nitrogen atom. Other elements that are contained in the four components of Spurr are C, O, and H. We recorded EEL spectra of ultrathin sections containing only the embedding medium and no cells. The films had a thickness of ∼25 nm. In the corresponding EEL spectra, only a high carbon ionization K-edge and an oxygen ionization K-edge were visible; no ionization K-edge of nitrogen and no impurities could be detected. In EEL spectra, the ionization K-edges of C and O can be found at energy losses of 284 and 532 eV, respectively.[29] The ionization K-edge of N in EEL spectra would be found at an energy loss of 401 eV.

Consequently, the nitrogen concentration in the embedding material is so low that it cannot be detected under the instrumental conditions used here; therefore, no falsifying influence of Spurr on the nitrogen distribution maps for the identification of CGP within the cells occurs.

For the preparation of the uranyl acetate specimens 2% (w/v) uranyl acetate in double-distilled water was dripped on a fine-meshed copper net of 1000 mesh. The solution was not completely sucked off, thereby

allowing the uranyl acetate to crystallize during subsequent drying in air. The recorded EEL spectra of these specimens showed only ionization edges of uranium, carbon, and oxygen. No nitrogen and no impurities could be detected in these specimens. In EEL spectra, uranium can be identified by the ionization $O_{4,5}$-edge at 96 eV, the $N_{6,7}$-edge at 381 eV, the N_5-edge at 738 eV, and the N_4-edge at 780 eV.[29]

Recording of Energy-Loss Images. To obtain nitrogen distribution images the three preedge images and one element-specific image from the specimens containing the bacterial cells were recorded as described above, applying an energy slit width of 20 eV. The positions of the energy windows were determined from an EEL spectrum, which contains a nitrogen ionization K-edge. Figure 1a shows the EEL spectrum of a boron nitride sample with a clearly visible nitrogen K-edge taken from the EEL reference handbook.[29] The energy-loss windows of the preedge windows are not allowed to overlap, because otherwise the measured intensities of the three images would be correlated. In addition, the preedge image closest to the edge onset of the element of interest should not overlap with the ionization edge. The nitrogen ionization edge can be found at an energy loss of 401 eV.[29] Therefore, we selected the following centers of the preedge energy-loss windows: 332, 357, and 382 eV.

The position of the energy-loss window for the element-sensitive image is usually selected in a way to detect as much of the intensity of the ionization edge as possible. Referring to Figure 1a an energy loss of 412 eV would be suitable. However, here it has to be considered that the specimens were stained with uranyl acetate. An EEL spectrum of an uranyl acetate sample is shown in Figure 1b for demonstration. The uranium $N_{6,7}$-edge starts at 381 eV and shows a local minimum at an energy loss of ~420 eV. At 450 eV the spectrum intensity increases again, and at an energy loss of ~530 eV the K-edge of oxygen is found. Setting the center of the energy slit at 412 eV for the element-specific image at a high concentration of uranium as concluded from Figure 1a would mean that the signal in the nitrogen distribution image would not only stem from nitrogen but also from uranium, because both considered ionization edges are very close together. To avoid this effect, the center of the energy-loss window of the element-specific image was set at an energy loss of 420 eV, where the ionization edge of uranium shows a local minimum (Figure 1b) and the ionization edge of nitrogen still shows a high intensity (Figure 1a).

In addition to the EEL spectrum of uranyl acetate, Figure 1b shows hatched areas, which represent the energy-loss windows at 332, 357, 382, and 420 eV with a width of 20 eV selected for detection of the preedge images and the element-specific image used for recording a nitrogen distribution map. The maximum of the U−$N_{6,7}$-edge lies within the energy-loss window at 382 eV. As a consequence, the background calculated from these images is too high. Since the energy-loss window of the element-sensitive image is positioned in the local minimum of the U−$N_{6,7}$-edge at 420 eV, the background calculated for the evaluation of the nitrogen signal remains too high in a worst case consideration if the uranium concentration is measurable. Therefore the calculated nitrogen signal in the nitrogen elemental map is definitely stemming from nitrogen and not from uranium and the obtained nitrogen signal in worst case is lower than the real signal would be. The overestimation of the background also leads to slightly negative signal intensities and signal-to-noise ratios in regions with low nitrogen concentrations (Figures 6−8).

Radiation Damage. Irradiation of organic specimens in the electron microscope can cause radiation damage, which is due to inelastic scattering processes of beam electrons at atoms of the sample. The energy transferred from the beam electrons can lead to the breakage of carbon chains in organic compounds. One consequence is a loss of mass.[24] For most embedding materials the residual mass shows an approximately exponential decrease down to a residual value as a function of electron dose, which is the product of current density and irradiation time. Further information about the mass loss as a function of electron dose is found in the literature.[24,38]

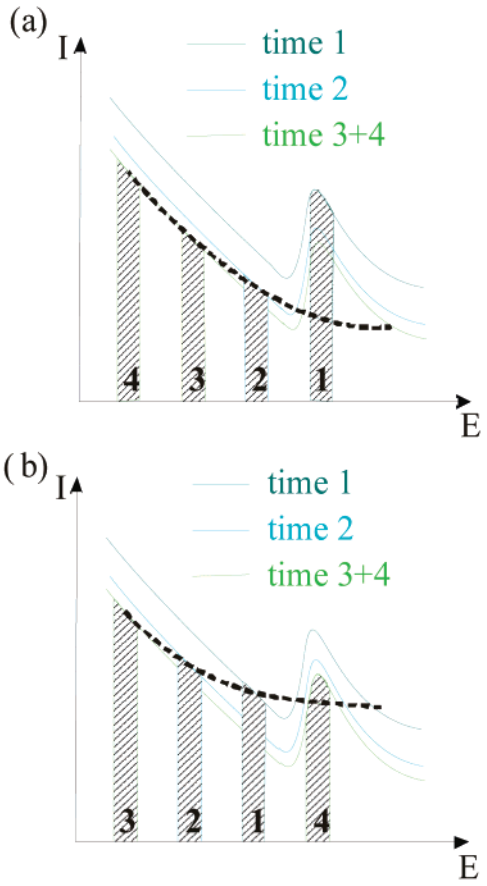

Figure 3. Schematic illustration of the effect of mass loss and of different orders of image recording (represented by the corresponding numbering) on the calculation of an element distribution image using an EEL spectrum: (a) recording of the element-sensitive image in the first place, followed by subsequent detection of the preedge images from high- to low-energy losses; (b) recording of the preedge images from high- to low-energy losses in the first place, followed by detection of the element-sensitive image. The effect of image recording at four given energy-loss ranges, referred to as energy windows, in different orders can be seen readily if comparing the windows 2 and 1 in part a with the corresponding windows 1 and 4 in part b, respectively. The differences in their heights reflect differences in the image intensity giving rise to different intensities of the element-specific images in parts a and b, which correspond to the red areas. Correcting the element-sensitive image for the background gives two different results for the signal of the element distribution image.

At a certain electron dose, the loss of mass starts being strong at the beginning and decreasing with increasing electron dose-. This information about the dependence of the mass loss on time at a constant current density is therefore used to decide in which order the preedge images and the element-specific image should be recorded when using the four-window method. Figure 3 provides a schematic illustration of the consideration, in which order the images should be recorded, and how this order influences the signal in an element distribution. Therefore, a schematic ionization edge is shown in Figure 3 at four different times. The intensity of the edge decreases with time due to the loss of mass, because the intensity depends on the number of scattering atoms. The mass loss is strong at the beginning, represented by the strong difference between the two intensities corresponding to the times 1 and 2. The loss of mass decreases with increasing electron dose; therefore, the distance between the intensities corresponding to times 2 and 3 is small. At a certain electron dose the mass loss is hardly measurable; therefore, the intensities corresponding to times 3 and 4 are identical (Figure 3).

Figure 3a corresponds to the case in which the element-sensitive image is recorded first, and afterward the preedge images are detected in order from high- to low-energy losses. The edge intensity at time 1

consequently corresponds to the recording of the element-sensitive image provided by the top line in Figure 3a. Using the preedge intensities for the calculation of the background and the extrapolation into the ionization edge area yields the background intensity, which has to be subtracted from the intensity of the element-sensitive image. This process is indicated by the dark broken curve. The resulting signal in the element distribution image is relatively high and can be compared to the case when there would be no mass loss. This case would be completely represented by the curve at the top referring to time 1 in Figure 3a. Calculating the background and performing the extrapolation into the ionization edge area would lead to a signal in the element distribution image, which is lower than that corresponding to the order of image recording explained above with measurable loss of mass. In the latter case, the signal in the element distribution image would be too high and hence falsified.

The result is different when we start with the recording of the preedge images from high- to low-energy losses and detect the element-sensitive image at the end, which is schematically shown in Figure 3b. Here the top curve at time 1 represents the recording of the preedge image closest to the onset of the ionization edge. In this case a background correction would lead to a signal in the element distribution image, which is lower as compared to the case shown in Figure 3a. The signal would even be lower than that in the case of no measurable loss of mass, where only the top curve of Figure 3b would have to be considered. Therefore, selecting the order of image recording as shown in Figure 3b would give a too low signal in the element distribution image, if there is a measurable loss of mass. Therefore, if there is a measurable loss of mass during the recording of the image series, then the order of image recording as illustrated in Figure 3b should be used, detecting the preedge images from high- to low-energy losses first and afterward the element-sensitive image. If there is a measurable loss of mass, then this would yield a too small signal in the element distribution image; however, it is certain that the residual signal is true and corresponds to the element of interest. This would not necessarily be the case when using the order of image recording as illustrated in Figure 3a in which the signal would be too high at a measurable loss of mass.

In this study, both orders of recording the image series were applied. To minimize the radiation damage when applying both orders of image recording, we first recorded the element-sensitive image at 420 eV and afterward the preedge images from high- to low-energy losses and finally again the element-sensitive image at 420 eV. This detection procedure comprises both orders of image recording and provided the advantage that the same preedge images can be used to calculate the background for both orders, and therefore the resulting background and the extrapolation error do not depend on the order of image recording. Consequently, not only the signal I_S of the element distribution image but also the SNR can be used for analyses, if there has been a measurable loss of mass during the recording procedure: When comparing both orders, a higher signal I_S corresponds to a higher SNR.

Since the intensities in the inelastically filtered images were very low at energy losses between 332 and 420 eV for the specimens analyzed in this study, the exposure time per image or alternatively the current density had to be increased. Because the mass loss as a function of electron dose should show approximately an exponential decrease, it is possible that the mass loss is very low or not measurable for such high doses.

Considerations on Sample Contaminations. Another factor that might influence the measurements is contamination of the samples during irradiation. During the contamination process, the ionization edge intensities of the contaminating materials increase, because according to eq 2 the edge intensity depends on the projected particle density. If the intensity of the carbon K-edge with an onset at 284 eV increases due to contamination, then the background of the nitrogen K-edge with an onset at 401 eV will therefore also increase. If this increase of background due to contamination is continuous during the recording of a series of inelastically filtered images, then the signal in a nitrogen map when first recording the preedge images from high- to low-energy losses and afterward detecting the element-sensitive image should be higher and more falsified as in the case of first detecting the element-sensitive image and then recording the preedge images from high- to low-energy losses. This effect is the same for the SNR when comparing both orders of image recording and using the same preedge images for the background calculation. The same preedge images can be used for both cases when we first record the element-sensitive image, continue with the detection of the preedge images from high- to low-energy losses, and finally record the element-sensitive image again, as done in this study. Therefore, in case of contamination, the order of recording the inelastically filtered images should be different from the order in the case of measurable mass loss as discussed above.

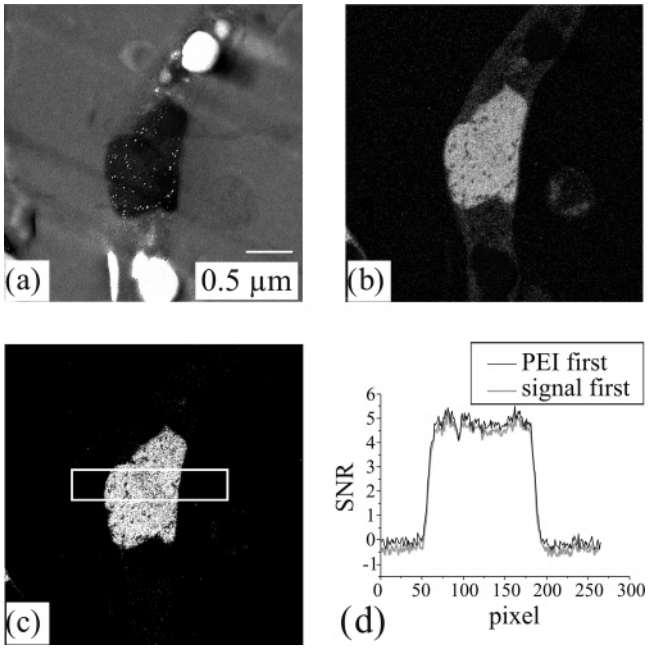

Figure 4. Analysis of *R. eutropha* H16 (pBBR1MCS-2::*cphA1*$_{7120}$) containing CGP and PHB granules: (a) elastically filtered image; (b) nitrogen distribution image of the same specimen area as in part a; (c) SNR image corresponding to part b; (d) averaged line scan (averaging in the vertical direction) within the area marked in part c for both orders of image recording. PEI: preedge image.

The following figures of this study present only element distribution images and SNR images resulting from first recording the preedge images from high- to low-energy losses and detecting the element-sensitive image at the end, because the optical appearance of these images of both recording orders did not differ very much. However, the SNR images were analyzed by line scans through the bacterial cells, and the results are presented in the corresponding figures and will be discussed for both orders of image detection.

Results

Analysis of Cells Accumulating Both CGP and PHB. Figure 4a shows the elastically filtered image of a *R. eutropha* H16 (pBBR1MCS-2::*cphA1*$_{7120}$) specimen having accumulated PHB and CGP with a thickness of ~30 nm. This cell contained a large dark granule with a size of ~0.75 × 1.25 μm^2 and in addition two bright inclusions with a maximum size of ~0.5 μm. In the nitrogen distribution image of this specimen area shown in Figure 4b, the large dark granule (Figure 4a) appeared bright. The height of the nitrogen signal in the nitrogen distribution map determines the brightness of the corresponding specimen area. Similarly, the higher the SNR is in the SNR image, the brighter the corresponding specimen area appeared (Figure 4c). Considering the Rose criterion, the contrast limits

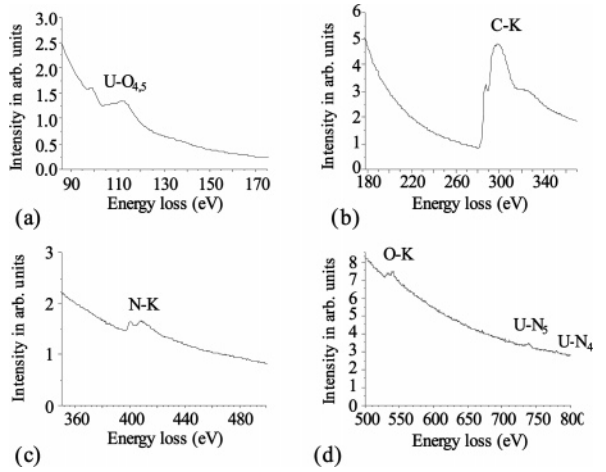

Figure 5. Analysis of *R. eutropha* H16 (pBBR1MCS-2::*cphA1*$_{7120}$) containing CGP and PHB granules: (a−d) parts of an EEL spectrum recorded on the specimen area of the granule, appearing dark in Figure 4a and bright in Figures 4b and 4c.

in the SNR image were set in such a way that a SNR < 3 appeared black and a SNR > 5 appeared white. Drawing a line scan in the nitrogen distribution image as indicated by the white line in Figure 4c and averaging it over a range of 50 pixels give the profiles of the SNR as a function of pixels for both discussed orders of image recording (Figure 4d). The dark profile refers to the order of first recording the preedge images from high- to low-energy losses and afterward the element-sensitive image ("PEI first", black line), whereas the bright profile refers to the second order of image recording ("signal first") starting with the detection of the element-sensitive image. These profile definitions and labels are kept in the following. Within the area corresponding to the dark granule of the elastically filtered image both profiles show SNR values between 4.5 and 5.5, which are remarkably higher than those in other areas. Similar data and profiles were obtained with specimen of other cells of *R. eutropha* H16 (pBBR1MCS-2::*cphA1*$_{7120}$).

By setting a suitable size and position of the filter entrance aperture of the imaging energy filter of the EFTEM and by investigating the same sample position as in Figure 4, a serial EEL spectrum of the specimen area only containing the granule, which appears dark in the elastically filtered image of Figure 4a, was recorded. The parts of the EEL spectrum showing ionization edges are illustrated in Figure 5. The $O_{4,5}$-edge of uranium starting at an energy loss of 96 eV is visible in Figure 5a. The uranium stems from the uranyl acetate that the specimen was stained with. The next observable ionization edge in the spectrum is the K-edge of carbon in Figure 5b, followed by the clearly visible nitrogen K-edge in Figure 5c. This edge has an onset at 401 eV. However, this edge cannot be confused with the $N_{6,7}$-edge of uranium, because the latter would show an onset at an energy loss of 381 eV;[29] in addition, its form is different: For example, the increase of intensity starting at an energy loss of ∼450 eV as in Figure 1b is missing. Therefore, the existence of nitrogen in the dark granule of Figure 4a is proven by this EEL spectrum. Figure 5d shows the ionization K-edge of oxygen and the uranium N_5- and N_4-edges.

Analysis of Cells Accumulating Only CGP. *R. eutropha* H16-PHB$^-$4 (pBBR1MCS-2::*cphA1*$_{7120}$) is unable to accumulate PHB due to a mutation in the genes for PHB biosynthesis. Therefore, the corresponding cells accumulated only cyanophycin, and PHB granules were absent as was confirmed by chemical analysis. Figure 6a shows the elastically filtered image of a sample of *R. eutropha* H16-PHB$^-$4 (pBBR1MCS-2::

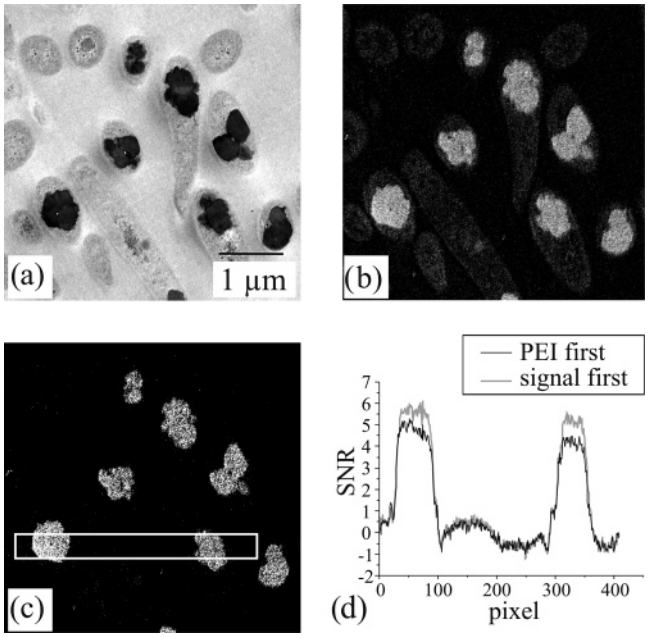

Figure 6. Analysis of *R. eutropha* H16-PHB$^-$4 (pBBR1MCS-2::*cphA1*$_{7120}$) containing only CGP but no PHB granules: (a) elastically filtered image; (b) nitrogen distribution image of the same specimen area as in part a; (c) SNR image corresponding to part b; (d) averaged line scan (averaging in the vertical direction) within the area marked in part c for both orders of image recording. PEI: preedge image.

cphA1$_{7120}$) with a thickness of ∼30 nm. Several cells are visible that contain granules appearing dark and exhibiting sizes between 0.25 and 0.75 μm. Brightly appearing inclusions as in Figure 4a, which represent PHB granules, could not be observed. In Figure 6b, the nitrogen distribution image of the same sample area as in Figure 6a is illustrated, showing bright granules, which correspond to the dark ones in the elastically filtered image of Figure 6a. These granules have a nitrogen signal that is higher by a factor of 9−10 than the nitrogen signal of the surrounding cell areas. Therefore, according to eq 2 the projected particle density of nitrogen in the granules has to be higher by the same factor as compared to the residual cell areas.

Figure 6c shows the SNR image corresponding to the nitrogen distribution map of Figure 6b. The contrast limits in Figure 6c were set in such a way that a pixel with a SNR < 3 appears dark, whereas a pixel with a SNR > 5 appears white. The granules in the SNR image corresponding to the dark granules of the elastically filtered image appeared bright and show a remarkably higher SNR than the residual cell areas. A line scan was drawn in Figure 6c, and the SNR within this line scan was averaged over a width of 40 pixels to compare the SNR within the granules with areas outside these granules. The corresponding profiles of the SNR as a function of pixels are presented in Figure 6d for both orders of image recording. These profiles show that the SNR within the dark granules of the elastically filtered image ranges from 4 to 6.

Analysis of Cells Accumulating Only PHB. So far we showed results for two recombinant strains of *R. eutropha*, which were provided with the gene for CGP biosynthesis. We also investigated cells lacking the gene for CGP biosynthesis to validate the results shown in Figures 4−6. The elastically filtered image of a sample of the wild-type of *R. eutropha*, capable of synthesizing PHB, is shown in Figure 7a. The specimen thickness of the analyzed samples was ∼30 nm. Several cells containing inclusions with diameters between 0.1 and 0.5 μm, which appear bright in the elastically filtered image, were visible (Figure 7a). Within the cell areas containing these

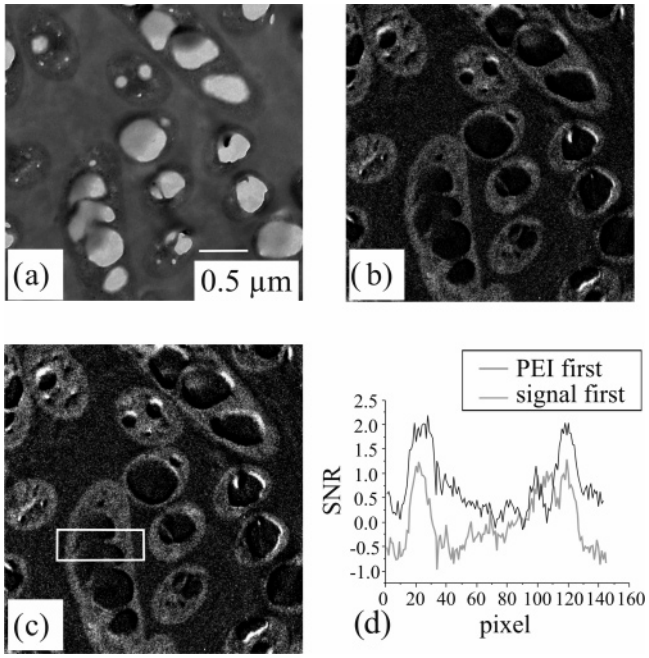

Figure 7. Analysis of *R. eutropha* H16 containing only PHB but no CGP granules: (a) elastically filtered image; (b) nitrogen distribution image of the same specimen area as in part a; (c) SNR image corresponding to part b; (d) averaged line scan (averaging in the vertical direction) within the area marked in part c for both orders of image recording. PEI: preedge image.

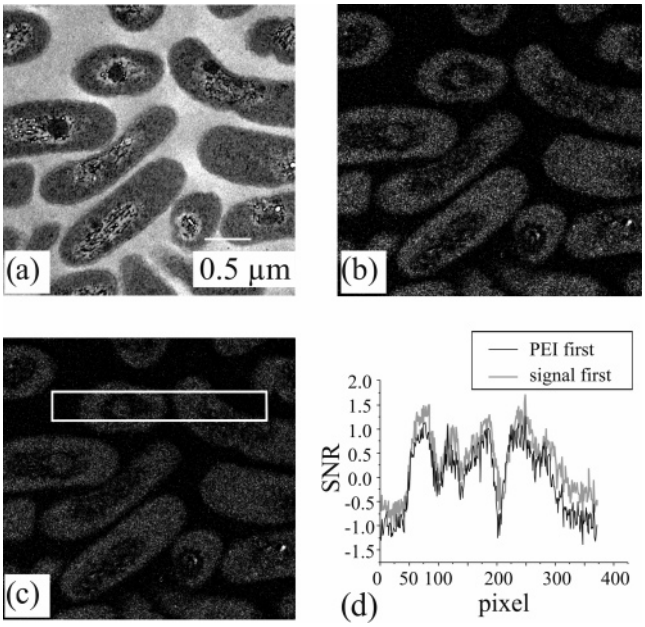

Figure 8. Analysis of *R. eutropha* H16-PHB$^-$4 containing neither CGP nor PHB granules: (a) elastically filtered image; (b) nitrogen distribution image of the same specimen area as in part a; (c) SNR image corresponding to part b; (d) averaged line scan (averaging in the vertical direction) within the area marked in part c for both orders of image recording. PEI: preedge image.

inclusions, the sample is very sensitive to irradiation and could be damaged or even destroyed within these areas during investigation by EFTEM. Figure 7b shows the nitrogen distribution image of the same specimen area as in Figure 7a. The bright granules in the elastically filtered image exhibited no nitrogen signal in the nitrogen map of Figure 7b and appeared black. Some edges of a few granules appeared white in Figure 7b; however, this is probably due to the damaging effect because of the sensitivity to irradiation of these granules as mentioned above. This damaging effect during the recording of the image series makes the granules change their form so that the preedge images and the element-sensitive image cannot be corrected completely for drift effects. Therefore, the white edges of the dark granules in Figure 7b are most probably not nitrogen signals but are caused by noncorrectable drift effects. The residual granule-free areas of the cells in Figure 7b show a small nitrogen signal due to nitrogen-containing compounds of the cell matter. Nitrogen-containing granules as observed with the two recombinant strains of *R. eutropha* accumulating CGP were absent in Figure 7b.

The SNR image corresponding to the nitrogen map of Figure 7b is illustrated in Figure 7c and shows only low SNR values in the granule-free cell areas. The contrast limits in Figure 7c were set in such a way that pixels with a SNR < 0 appear black whereas pixels with a SNR > 5 appear white to see these small SNR values. A line scan was drawn in the SNR image within a cell area containing a granule, and the intensities were averaged within a width of 50 pixels. The corresponding profile of the SNR as a function of image pixels is shown for both orders of image recording (Figure 7d). The SNR decreases to values of about zero within the area of the PHB granule, while outside the granule comprising the surrounding cell matter a SNR of $\sim 1-2$ is observed.

Analysis of Cells without CGP and PHB Inclusions. Figure 8a shows the elastically filtered image of a sample of the PHB-negative mutant *R. eutropha* H16-PHB$^-$4 with a specimen thickness of $\sim 25-30$ nm. These cells were incapable of accumulating either polymer, and the cells therefore did not contain bright or dark granules. Some of the cells contained dark round areas with diameters of ~ 0.2 μm. In the nitrogen distribution image presented in Figure 8b, these areas did not exhibit a higher nitrogen signal than the other cell areas, which show a visible but weak nitrogen signal. The SNR image referring to the nitrogen map is illustrated in Figure 8c, revealing only a low SNR value corresponding to the small nitrogen signal of Figure 8b. The contrast limits of Figure 8c were set in such a way that pixels with a SNR < 0 appeared black and pixels with a SNR > 5 appeared white. A line scan was drawn in the SNR image containing two round dark features of the elastically filtered image of Figure 8a, and the SNR values were averaged over a width of 50 pixels. The corresponding profile of the SNR as a function of pixels is shown in Figure 8d. The maximum SNR was ~ 1.5 within this averaged line scan, and the areas, which appeared dark in the elastically filtered image, did not show a higher SNR value than the other cell areas corresponding to visible nitrogen signals in Figure 8b.

Discussion

The higher the nitrogen signal is in the nitrogen distribution map, the brighter the corresponding specimen area appears in this image. Consequently the dark granule in the elastically filtered image of the *R. eutropha* H16 (pBBR1MCS-2:: $cphA1_{7120}$) sample of Figure 4a shows a nitrogen signal in the corresponding nitrogen distribution image of Figure 4b, while the two smaller granules are bright in the elastically filtered image but do not contain a nitrogen signal. The rest of the cell area only has a small nitrogen signal in Figure 4b. For both orders of image recording the nitrogen signal of Figure 4b corresponding to the dark granule of Figure 4a is by a factor of $5-6$ higher than that of the inclusion-free surrounding cytoplasm. According to eq 2 the characteristic nitrogen intensity depends on the projected particle density of nitrogen. Therefore,

the concentrations of nitrogen in the granules and in the cytoplasm should differ also by this factor.

Figures 4c and 4d show that the granule corresponding to the dark inclusion of Figure 4a appears bright in the SNR image and has a SNR value per pixel of ~4.5−5.5. According to the Rose criterion, nitrogen was considered to be identified at a SNR ≥ 5, if we have no previous knowledge about the specimen. However, we have additional information about this granule provided by the EEL spectrum (Figure 5) recorded of the specimen area only containing this granule that shows very clearly the nitrogen K-edge. Consequently, the granule must be enriched with nitrogen compounds. Furthermore, using the knowledge that nitrogen is contained in the sample would only take a SNR ≥ 3 for an identification of nitrogen in a pixel when applying the Rose criterion. So the nitrogen is proven within the dark granule of Figure 4a of the *R. eutropha* H16 (pBBR1MCS-2::*cphA1*$_{7120}$) sample. It cannot be proven in the bright granules of Figure 4a, because these granules are not visible in the SNR image in Figure 4c, where the contrast limits have been set so that SNR < 3 appears black. Considering that cells of *R. eutropha* H16 (pBBR1MCS-2::*cphA1*$_{7120}$) contain CGP and that CGP has a remarkably higher nitrogen content than the cell dry matter, we conclude that the dark granule in the elastically filtered image contains CGP. Comparing the nitrogen content in CGP to that of the cell dry matter, one would expect a factor of only 2. The reason for measuring a factor of 5−6 might be the high density of CGP in the granule because the density should parallel the projected density of atoms in the illuminated sample volume, thus yielding a higher signal in the nitrogen map according to eq 2. This compactness is probably due to the lower water content of the granules as compared to the cytoplasm.

Representatives of the second type of inclusion in the cells were bright in the elastically filtered image (Figure 4a), did not give a visible nitrogen signal (Figure 4b), and were very sensitive to radiation, thus yielding damaged areas when applying a too high irradiation. Since *R. eutropha* H16 (pBBR1MCS-2::*cphA1*$_{7120}$) synthesizes not only CGP but also PHB, which does not contain nitrogen, it is very likely that these granules, which are bright in the elastically filtered image, contain PHB. The absence of such bright granules in the elastically filtered images of cells of the PHB-negative mutant *R. eutropha* H16-PHB^{-}4 (pBBR1MCS-2::*cphA1*$_{7120}$) strongly supported this assumption.

In cells of *R. eutropha* H16-PHB^{-}4 (pBBR1MCS-2::*cphA1*$_{7120}$), such bright inclusions were absent in elastically filtered images (Figure 6a), and only dark granules with SNR values between 4 and 6 and similar other features like those in *R. eutropha* H16 (pBBR1MCS-2::*cphA1*$_{7120}$) were found (Figures 6c and 6d). Therefore, the existence of nitrogen in these types of granules was proven. Because *R. eutropha* H16-PHB^{-}4 (pBBR1MCS-2::*cphA1*$_{7120}$) accumulates CGP and since the dark granules in the elastically filtered images contained much more nitrogen than the residual areas of the cells, it was concluded that these dark granules contain CGP. The fact that the nitrogen signal in the granules of Figure 6b was 9- to 10-fold and not only 2-fold higher as compared to the surrounding cytoplasm might be attributed again to the higher density of CGP in the granules as discussed above.

To validate these results obtained with *R. eutropha* H16 (pBBR1MCS-2::*cphA1*$_{7120}$) and *R. eutropha* H16-PHB^{-}4 (pBBR1MCS-2::*cphA1*$_{7120}$), cells of the wild-type (strain H16) and of the PHB-negative mutant (strain H16-PHB^{-}4) of *R. eutropha*, which do not have foreign genes and accumulate only PHB (Figure 7) or no PHB (Figure 8), respectively, were also analyzed. In the wild-type we only detected bright granules in the elastically filtered image (Figure 7a), which did not exhibit a nitrogen signal in the nitrogen distribution image (Figure 7b). The corresponding SNR values in the SNR image of Figure 7c are very low and close to zero, thus indicating that nitrogen is absent from these granules. Since this strain of *R. eutropha* accumulates only PHB, we can conclude that these bright granules in the elastically filtered image contain PHB. The granule-free areas of the cells of *R. eutropha* H16 (Figure 7) and of *R. eutropha* H16-PHB^{-}4 (Figure 8) show a low nitrogen signal with SNR values between 1 and 2, which can be attributed to the nitrogen share of 6.8% at the atomic level of the cell matter.

The dark round areas in the elastically filtered images of the PHB-negative cells showed only weak nitrogen signals and low SNR values, which were comparable to those of PHB and CGP granule-free areas of the other strains investigated in this study. They were not comparable to the dark granules in the elastically filtered images of *R. eutropha* H16 (pBBR1MCS-2::*cphA1*$_{7120}$) and *R. eutropha* H16-PHB^{-}4 (pBBR1MCS-2::*cphA1*$_{7120}$), which represented CGP granules and which showed generally remarkably higher nitrogen signal and SNR values. Bright granules representing PHB also could not be detected in the elastically filtered images of *R. eutropha* H16-PHB^{-}4 (Figure 8a).

Since no nitrogen-enriched granules were found in the strains *R. eutropha* H16 and *R. eutropha* H16-PHB^{-}4, which do not contain foreign genes for CGP biosynthesis, the results of Figures 4−7 for the recombinant strains of *R. eutropha* H16 (pBBR1MCS-2::*cphA1*$_{7120}$) and *R. eutropha* H16-PHB^{-}4 (pBBR1MCS-2::*cphA1*$_{7120}$) are validated, identifying CGP as dark granules in the elastically filtered images due to their high nitrogen signal in the corresponding nitrogen distribution images and due to the corresponding SNR.

Conclusions

Element distribution images and EEL spectra were recorded by an energy-filtering transmission electron microscope to identify in situ the localization of nitrogen-containing CGP in recombinant strains of *R. eutropha*. The EEL spectra recorded on specimens of the embedding medium Spurr and the staining material uranyl acetate, the bacterial cells were treated with, showed no impurities and no nitrogen signals; therefore, both compounds do not falsify the nitrogen signals in EEL spectra of the bacterial cells. However, the ionization $N_{6,7}$-edge of uranium in uranyl acetate reduced the choice for the energy-loss windows of preedge images and of the element-sensitive images for nitrogen maps. Therefore, the energy-loss window for the element-sensitive image has to be positioned at a sufficient distance from the $N_{6,7}$-edge of uranium, and the energy-loss window for the preedge image closest to the nitrogen K-edge has to be centered within a local maximum of the uranium $N_{6,7}$-edge to ensure that no uranium signal is interpreted as a nitrogen signal.

Because a loss of mass in the sample or contamination during the recording of the inelastically filtered image series should have an influence on the nitrogen signal in a nitrogen distribution image, two orders of recording the images were applied, both yielding corresponding results for the analysis of the nitrogen maps. The first sequence started with the recording of the preedge images from high- to low-energy losses and finished with the detection of the element-sensitive image. The second sequence started with the recording of the element-sensitive

image and finished with the detection of the preedge images from high- to low-energy losses. This method allows for the first time imaging of the distribution of CGP in the cytoplasm. So far various light and electronic microscopic methods have been used to identify CGP granules in cells. (for a review, see ref 39) The method applied in this study will beside the various microscopic methods provide an additional method not only to identify CGP granules in situ in cells but also to discriminate them from other insoluble inclusions in the cells such as PHAs, lipids, polyphosphates, or glycogen granules, which are distinguished from CGP by their element composition.

Possible applications of element distribution images might be the analytical analysis of membranes covering granules and cells as well as interior components of individual cells and nuclei rich in phosphorus or sulfur (e.g., refs 40−42). Mapping of the locations of physiologically significant ions, ion shifts related to dynamic processes within cells, and trace element analysis at nanoscale resolution could be another important application (e.g., ref 43) The success of such an analysis is strongly dependent on the type and the edge onset of the ionization edge used for the analysis for the element of interest, the concentration of the element in the membrane, the thickness of the membrane, the radiation sensitivity of the specimen, and the performance of the electron microscope used for this analysis. Elements revealing only practically usable ionization edges with a delayed edge intensity maximum at high-energy losses in EEL spectra are harder to detect in element distribution images than elements revealing practically usable ionization edges with strong edge onsets at energy losses up to 700 eV. For the Zeiss EM 902 EFTEM used here for the experiments, structures containing nitrogen with a share of ∼5 at. % are hard to resolve in nitrogen distribution maps if they have dimensions less than 10−15 nm and if the specimen is radiation-sensitive, which is a problem when recording a series of images on the same sample area.

Acknowledgment. We thank Mrs. Ursula Malkus (Institut für Medizinische Physik und Biophysik) for expert electron microscopic preparation of the specimens. This study was supported by grants provided by the Bundesministerium für Verbraucherschutz, Ernährung and Landwirtschaft (00NR125) and Bayer AG (Leverkusen, Germany).

References and Notes

(1) Borzi, A. *Malpighia* **1887**, *1*, 28.
(2) Simon, R. D.; Weathers, P. *Biochim. Biophys. Acta* **1976**, *420*, 165.
(3) Allen, M. M. *Annu. Rev. Microbiol.* **1984**, *38*, 1.
(4) Allen, M. M. *Methods Enzymol.* **1988**, *167*, 207.
(5) Allen, M. M.; Hutchinson, M. F.; Weathers, P. J. *J. Bacteriol.* **1980**, *141*, 687.
(6) Simon, R. D. *Proc. Natl. Acad. Sci. U.S.A.* **1971**, *68*, 265.
(7) Simon, R. D. *Acta Biochim. Biophys.* **1976**, *422*, 407.
(8) Simon, R. D. In *The Cyanobacteria*; Fay, P., van Baalen, C., Eds; Elsevier: Amsterdam, The Netherlands, 1987; p 199.
(9) Lawry, N. H.; Simon, R. D. *J. Phycol.* **1982**, *18*, 391.
(10) Krehenbrink, M.; Oppermann-Sanio, F. B.; Steinbüchel, A. *Arch. Microbiol.* **2002**, *177*, 371.
(11) Mackerras, A. H.; De Chazal, N. M.; Smith, G. D. *J. Gen. Microbiol.* **1990**, *136*, 2057.
(12) Joentgen, W.; Groth, T.; Steinbüchel, A.; Hai, T.; Oppermann, F. B. International Patent Application WO 98/39090, 1998.
(13) Steinbüchel, A.; Hai, T.; Oppermann, F. B.; Joentgen, W.; Groth, T. German Patent Application Le A 32341, 1997.
(14) Schwamborn, M. *Polym. Degrad. Stab.* **1998**, *59*, 39.
(15) Ziegler, K.; Diener, A.; Herpin, C.; Richter, R.; Deutzmann, R.; Lockau, W. *Eur. J. Biochem.* **1998**, *254*, 154.
(16) Voss, I.; Diniz Cardoso, S.; Aboulmagd, E.; Steinbüchel, A. *Biomacromolecules* **2004**, *5*, 1588.
(17) Oppermann-Sanio, F. B.; Hai, T.; Aboulmagd, E.; Hezayen, F. F.; Jossek, S.; Steinbüchel, A. In *Biochemical Principles and Mechanisms of Biosynthesis and Biodegradation of Polymers*; Steinbüchel, A., Ed.; Wiley-VCH: Weinheim, Germany, 1999; p 185.
(18) Aboulmagd, E.; Oppermann-Sanio, F. B.; Steinbüchel, A. *Arch. Microbiol.* **2000**, *174*, 297.
(19) Berg, H.; Ziegler, K.; Piotukh, K.; Baier, K.; Lockau, W.; Volker-Engert, R. *Eur. J. Biochem.* **2000**, *267*, 5561.
(20) Hai, T.; Oppermann-Sanio, F. B.; Steinbüchel, A. *FEMS Microbiol. Lett.* **1999**, *181*, 229.
(21) Ziegler, K.; Deutzmann, R.; Lockau, W. *Z. Naturforsch.* **2002**, *57*, 522.
(22) Aboulmagd, E.; Voss, I.; Oppermann-Sanio, F. B.; Steinbüchel, A. *Biomacromolecules* **2001**, *2*, 1338.
(23) Reimer, L. In *Energy-Filtering Transmission Electron Microscopy*; Reimer, L., Ed.; Springer Series in Optical Sciences 71; Springer: Berlin, Germany, 1995; p 347.
(24) Reimer, L. *Transmission Electron Microscopy: Physics of Image Formation and Microanalysis*, 4th ed.; Springer Series in Optical Sciences 36; Springer: Berlin, Germany, 1997.
(25) Schlegel, H. G.; Kaltwasser, H.; Gottschalk, G. *Arch. Mikrobiol.* **1961**, *28*, 209.
(26) Friedrich, B.; Hogrefe, C.; Schlegel, H. G. *J. Bacteriol.* **1981**, *147*, 198.
(27) Romeis, B. *Mikroskopische Technik*; Oldenburg-Verlag: Wien, Austria, 1968.
(28) Spurr, A. R. *J. Ultrastruct. Res.* **1969**, *26*, 31.
(29) Reimer, L.; Zepke, U.; Moesch, J.; Schulze-Hillert, S.; Ross-Messemer, M.; Probst, W.; Weimer, E. *A Reference Handbook of Standard Data for Identification and Interpretation of Electron Energy Loss Spectra and for Generation of Electron Spectroscopic Images*; Carl Zeiss, Electron Optics Division: Oberkochen, Germany, 1992.
(30) Egerton, R. F. *Electron Energy-Loss Spectroscopy in the Electron Microscope*; Plenum Press: New York, 1996.
(31) Egerton, R. F.; Leapman, R. D. Q. In *Energy-Filtering Transmission Electron Microscopy*; Reimer, L., Ed.; Springer Series in Optical Sciences 71; Springer: Berlin, Germany, 1995; p 269.
(32) Müller, I. Einsatz eines Multivariaten Analyseverfahrens zur Segmentierung von Elementverteilungsbildern. Ph.D. Thesis, University of Münster, Münster, Germany, 2001.
(33) Pun, T.; Ellis, J. R.; Eden, M. *J. Microsc.* **1985**, *137*, 93.
(34) Unser, M.; Ellis, S. R.; Pun, T.; Eden, M. *J. Microsc.* **1987**, *145*, 245.
(35) Rose, A. *Image Technol.* **1970**, *12*, 13 and 30.
(36) Natusch, M. K. H.; Humphreys, C. J.; Menon, N.; Krivanek, O. L. *Micron* **1999**, *30*, 173.
(37) Steinbüchel, A.; Aerts, K.; Babel, W.; Föllner, C.; Liebergesell, M.; Madkour, M. H.; Mayer, F.; Pieper-Fürst, U.; Pries, A.; Valentin, H. E.; Wieczorek, R. *Can. J. Microbiol.* **1995**, *41* (Suppl. 1), 94.
(38) Reichelt, R.; Carlemalm, E.; Villiger, W.; Engel, A. *Ultramicroscopy* **1985**, *16*, 69.
(39) Obst, M., Steinbüchel, A. In *Inclusions in Prokaryotes*; Shively, J. M., Ed.; Springer Microbiology Monograph Series; Springer: Berlin, Germany, 2006; p 167.
(40) Abolhassani-Dadras, S.; Mayer, J.; Vazquez-Nin, G. H.; Fakan, S. In *Proceedings of the 14th International Congress on Electron Microscopy*; Benavides, H. A. C., Yacaman, M. J., Eds.; Institute of Physics Publishing: Bristol, U. K., 1998; Vol. 1, p 687.
(41) Leapman, R. D.; Jarnik, M.; Steven, A. C. In *Proceedings of the 14th International Congress on Electron Microscopy*; Benavides, H. A. C., Yacaman, M. J., Eds.; Institute of Physics Publishing: Bristol, U. K., 1998; Vol. 1, p 689.
(42) Vazquez-Nin, G. H.; Echeverria, O.; Abolhassani-Dadras, S.; Boutinard-Rouelle-Rossier, V.; Fakan, S. In *Proceedings of the 14th International Congress on Electron Microscopy*; Benavides, H. A. C., Yacaman, M. J., Eds.; Institute of Physics Publishing: Bristol, U. K., 1998; Vol. 1, p 691.
(43) Leapman, R. D.; Newbury, D. E. *Anal. Chem.* **1993**, *65*, 2409.
(44) Schlegel, H. G.; Lafferty, R.; Krauss, I. *Arch. Mikrobiol.* **1970**, *71*, 283.
(45) Kovach, M. E.; Elzer, P. H.; Hill, D. S.; Robertson, G. T.; Farris, M. A.; Roop, R. M.; Peterson, K. M. *Gene* **1995**, *166*, 175.

BM0611230

CDV